Citation
Yuan, C. and Kong, Q. and Chen, W. and Jiang, J. and Hao, H. 2020. Interfacial debonding detection in externally bonded bfrp reinforced concrete using stress wave-based sensing approach. Smart Materials and Structures. 29 (3): ARTN 035039. http://doi.org/10.1088/1361-665X/ab7111

Interfacial Debonding Detection in Externally Bonded BFRP Reinforced Concrete Using Stress Wave-based Sensing Approach

Cheng Yuan[1], Qingzhao Kong[1,2], Wensu Chen[1,*], Jiafei Jiang[2], Hong Hao[1,*]

[1]*Centre for Infrastructural Monitoring and Protection, School of Civil and Mechanical Engineering, Curtin University, Australia*
[2]*Department of Disaster Mitigation for Structures, Tongji University, Shanghai, China*
**Corresponding Authors*

Abstract

Fibre-reinforced polymer (FRP) composite materials have been increasingly used for strengthening concrete members. The strengthening performance and structural capacity of FRP reinforced concrete structures are highly influenced by the interfacial bonding behaviour between FRP and concrete. A reliable technique for debonding detection, especially at its early age, is essential to ensure the strengthening efficacy and avoid premature failure of FRP reinforced concrete structures. This study develops a stress wave-based sensing approach to quantitatively monitor the debonding process by using surface mounted piezoceramic-based transducers (also called as smart aggregates SAs). The scanning wave signals in swept frequency mode and single frequency mode were utilized in experimental and numerical methods, respectively. Both results showed that when the stress wave propagated through the FRP-concrete interface, the wave energy attenuation increased as the debonding developed. To quantify the debonding level and provide assessment of the interface condition, a wavelet packet-based debonding index was established and its validity was verified by the data retrieved from digital image correlation (DIC) measurement. The proposed method has potential for fast determination or real-time monitoring of FRP-concrete interfacial debonding for both research and field applications.

Keywords: BFRP composite, debonding detection, piezoceramic, smart aggregate, guided wave.

1. Introduction

Fibre reinforced polymer (FRP) sheet has sound mechanical properties and it has been widely applied to strengthen existing reinforced concrete (RC) structures [1-3]. Due to environmental-induced aging or damage, and improper design caused defects, externally bonded (EB) FRP sheet has been considered as one of the most effective methods for strengthening and retrofitting of RC structures in flexural, shear, and confinement [4-6]. The efficiency of EB FRP strengthening performance is governed by the interfacial bonding condition between FRP sheet and concrete [7]. FRP debonding caused by concrete cover separation, sheet end delamination, or intermediate flexural crack-induced interfacial debonding is the most critical issue for the performance of FRP strengthening, which also influences the interfacial contact stiffness between FRP and concrete [8]. The interfacial shear resistance could be undermined because of local bond-slip caused by concrete cracking or debonding [2, 9].

A few methods of debonding detection have been proposed to quantify the interfacial damage caused by the local cracks in concrete and local bond-slip between FRP and concrete. For the interfacial debonding detection, the existing techniques mainly include strain gauge measurement and imaging technology [10, 11]. Externally mounted strain gauge measurement is a conventional way to obtain the strain development on FRP surface. However, strain gauges might be easily damaged during operating, and the measured results could be affected by the workmanship. Furthermore, mounted strain gauges cannot be removed or reused, which results in the increased cost for laboratory research and field applications. Alternatively, digital image correlation (DIC) technique, as a contactless measurement method, has shown potentials to replace the conventional contact-measuring method. Successive digital images can be recorded, and the full-field displacement and strain can be analysed from surface speckles tracked by the

DIC system [12]. It has been demonstrated that the DIC technique exhibits the great accuracy with an acceptable cost [13, 14]. However, the DIC technique is not suitable for long-term measurement due to large amounts of data to be stored.

On the other hand, wave-based methods have been widely used for target detection, classification, localization, and prediction in engineering practice [15-17]. Ong et al. [16] proposed a technique for detecting lap joints based on lamb wave technology and found that the proposed method had the potential to identify the presence of debonding in an adhesive-bonded joint. In recent years, there is an increasing use of acoustic wave as a non-invasive tool for health monitoring and condition assessment of civil structures [18]. It has been demonstrated that the acoustic-based (active or passive) damage detection technique is an effective way to detect cracks and holes of composite enclosures and also measure the vibroacoustic flexibility matrix of damaged surface of aluminium enclosures [19, 20].

In this study, a stress wave-based sensing approach was developed to detect the interfacial debonding of the BFRP-concrete interface in real time. A single-lap shear test specimen was prepared to simulate the debonding process. Two pairs of piezoceramic-based transducers called smart aggregates (SAs) were mounted on the concrete side and the FRP side to excite and detect the stress wave signals, respectively. During the course of loading, two SA actuators on the concrete side periodically generated the designed stress wave signal in swept frequency mode, which propagated through the BFRP-concrete interface and was detected by the paired SA sensors. The experimental results showed that when the stress wave propagated through the BFRP-concrete interface, the wave energy attenuation increased as the debonding developed. This phenomenon was also observed and verified in the numerical study. A wavelet packet-based debonding damage index was developed to quantify the debonding level at the local area where the SA sensors were placed. The debonding levels at the location of SA

sensors computed from the debonding damage index were compared with the local shear slips that obtained from the DIC system.

2. Methodology

2.1 Stress wave scanning using smart aggregates

Piezoelectric Lead Zirconate Titanate (PZT) transducers have emerged as one of the most popular devices for wave signal generation and detection due to their low cost, quick installation, wide frequency range, and high sensitivity [21, 22]. To ensure the survivability of fragile PZT material, smart aggregate (SA) transducer was used in this study. The SA was designed as a sandwiched structure by protecting PZT patch with two marble blocks, as shown in Figure 1 (a-b). The reliability, functionality, and feasibility of using SAs for SHM projects have been proven in the past ten years [23].

In this study, two pairs of SAs were used to detect the interfacial debonding at two locations along the BFRP sheet. The schematic diagram of the sensing approach using SA enabled stress wave for the debonding detection of the externally bonded BFRP reinforced concrete is given in Figure 1 (c-d). For each pair of SAs, the one marked with red colour functions as a generator to emit a designed stress wave signal from the concrete side to the BFRP side. The other one on the BFRP side functions as a receiver to detect the propagated stress wave. When debonding damage occurs, the existence of the gap which acts as an additional interface will cause amplified wave reflection. Therefore, the stress wave attenuation from concrete side to BFRP side increases correspondingly as debonding intensifies.

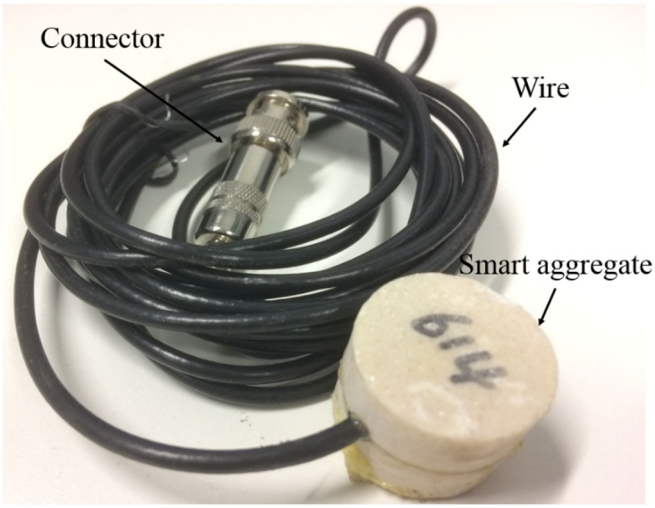

(a) The photo of smart aggregate

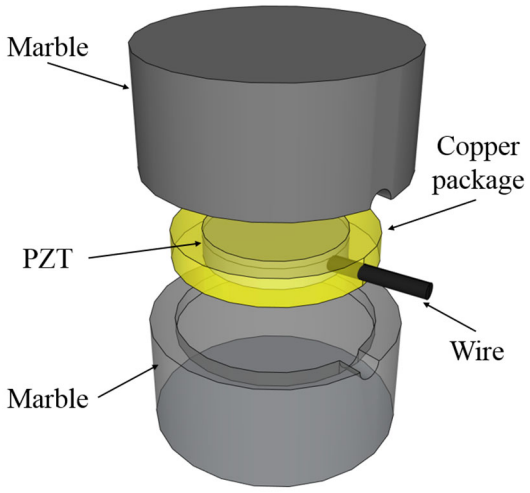

(b) The sketch of smart aggregate

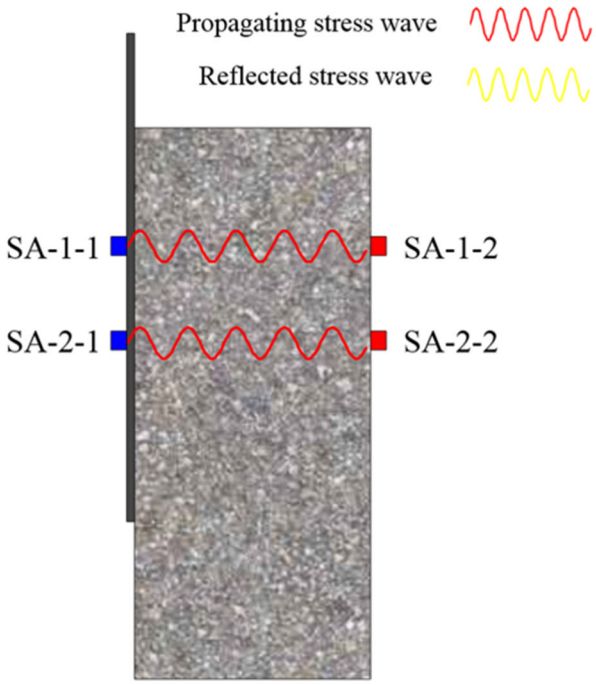

(c) Pre-debonding

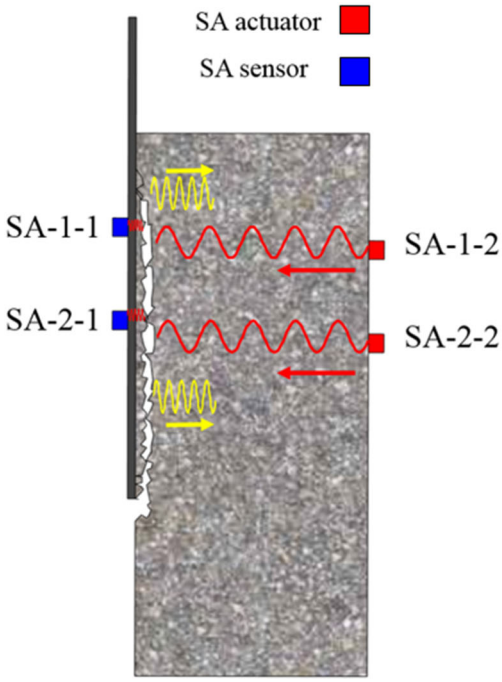

(d) Post-debonding

Figure 1. The diagrams of smart aggregate (SA) and debonding detection using stress wave scanning

2.2 Debonding damage index

To define the debonding induced stress wave energy loss and quantify the debonding condition of the BFRP-to-concrete interface, a wavelet packet-based debonding damage index was adopted in this study. Wavelet analysis has been widely used as an effective signal processing tool in the field of structural health monitoring [23, 24]. In this study, wavelet packet

decomposition divides the sensor signal Y into 2^n signal sets $\{Y_1, Y_2, \cdots, Y_j, \cdots, Y_{2^n}\}$, in which j is the frequency of band at the n-level decomposition ($j = 1, \cdots, 2^n$), and Y_j can be represented by Equation (1):

$$Y_j = \left[y_{j,1}, y_{j,2}, \cdots, y_{j,m} \right] \tag{1}$$

where m is the data samplings. The energy E_j of the decomposed signal Y_j is defined by Equation (2):

$$E_j = \left\| Y_j \right\|^2 = y_{j,1}^2 + y_{j,2}^2 + \cdots + y_{j,m}^2 \tag{2}$$

The energy vector $E_{i,j}$ of the sensor signal Y_i, where i refers to the i^{th} measurement, is defined by Equation (3):

$$E_{i,j} = \left[E_{i,1}, E_{i,2}, \cdots, E_{i,2^n} \right] \tag{3}$$

The energy vector $E_{0,j}$, as a baseline, is retrieved from the measurement on the healthy state of the BFRP-to-concrete interface. The debonding damage index I is defined by Equation (4):

$$I = \sqrt{\frac{\sum_{j=1}^{2^n} (E_{i,j} - E_{o,j})^2}{\sum_{j=1}^{2^n} {E_{o,j}}^2}} \tag{4}$$

The debonding damage index (I) refers to the energy attenuation caused by the debonding between BFRP sheet and concrete. When the bonding condition is in healthy state, the values of $E_{0,j}$ and $E_{i,j}$ are very close to each other, therefore the damage index value remains zero. The increase of the debonding index value corresponds to the increase of the stress wave attenuation ratio at the BFRP-concrete interface. If the BFRP sheet is entirely debonded from concrete at the sensor location, the sensor will not detect any stress wave energy from the

actuator. Therefore, the debonding damage index value is one as $E_{i,j}$ in this state is close to zero.

3. Experimental setup

3.1 Test specimen and SA location

In this study, a concrete block with compressive strength of 40 MPa was prepared for the single-lap shear test. The dimensions of the prepared concrete block were 150 x 150 x 350 mm. Two layers of BFRP sheets with the density of 300 g/m^2 were bonded onto the surface of concrete prism. The rupture tensile strength, elastic modulus, and failure strain of the BFRP sheet were measured as 1333 MPa, 73 GPa, and 0.l9%, respectively. The adhesive used to saturate the fibre is two-component epoxy resin at a weight ratio of 5:1. The ultimate tensile strength, elastic modulus, and rupture strain of the adhesive provided by the manufacturers were 50.5 MPa, 2.8 GPa, and 4.5%, respectively.

Figure 2 shows the details of the single-lap specimen and the location of SAs. SA-1-1 and SA-2-1 were used as receivers while SA-1-2 and SA-2-2 were set to be actuators, respectively. The SA-1-1 and SA-1-2 pair was placed near the loaded end to detect the early debonding. The SA-2-1 and SA-2-2 pair was placed 40 mm away from the SA-1-1 and SA-1-2 to detect the debonding within the effective bond length (EBL). EBL refers to the bond length of BFRP sheet over which there is no debonding resistance. By means of two pairs of SAs, debonding failure at two SAs' locations can be monitored in real time.

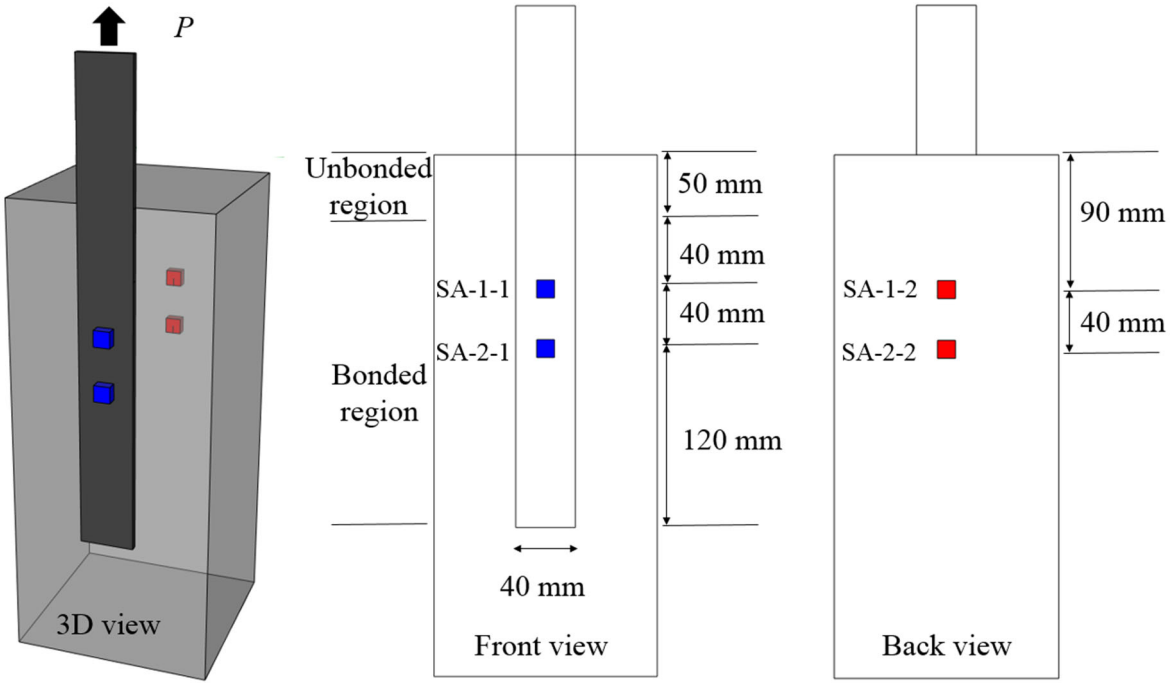

Figure 2. Specimen details

3.2 Testing facilities

In the test, the concrete block was fixed by a designed steel fixture on the workbench and tensile loading was applied on the loading end of BFRP. The debonding load was measured by a built-in load cell of the universal testing machine. The testing facilities are shown in Figure 3, which include two pairs of SAs (i.e., four SAs), data acquisition system (NI-USB6366), laptop, testing machine and DIC camera. During the tensile loading, both SA actuators on concrete side periodically generated the designed stress wave signal in swept frequency mode, which propagated through the BFRP-concrete interface and was detected by the paired SA sensors. The amplitude, start frequency, stop frequency and the sweeping period of the swept sine wave signal was 10 V, 1 kHz, 300 kHz, and 1 s, respectively. The sampling rate of the data acquisition system for each channel was 2 MHz.

2D Digital image correlation (2D-DIC) technique was used to measure the full-field displacement and strain of the BFRP sheet. The measured surface strain was used to obtain the interfacial shear stress and the local bond-slip was consequently obtained. The shear slip of the

BFRP sheet was measured by the DIC technique and the relationship between debonding damage index and shear slip was established accordingly.

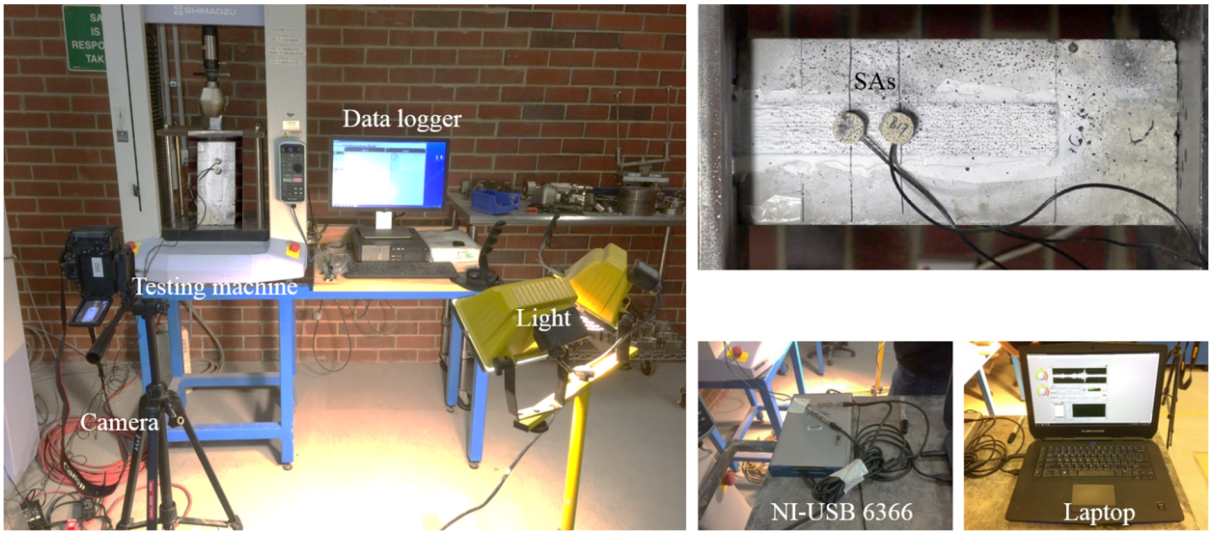

Figure 3. Test setup

4. Experimental results

4.1 Debonding load and shear slip

Figure 4 illustrates the load-slip response and load-time history, respectively. It was observed that the debonding load of the tested specimen was around 12 kN. Three regions can be observed for the interfacial load-slip curves, as shown in Figure 4. At the initial stage OA, the shear slip between BFRP sheet and concrete was small and this stage was defined as the elastic region. With the increase of the applied load, the shear slip increased gradually in the stage AB, which was resulted from the microcracking of concrete. As shown in Figure 4 (b), the initial debonding initiated at the instant of 450 s, i.e. point B. After reaching the initial debonding point B, the shear slip increased sharply while the applied load almost remained constant during the debonding process of the stage BC as shown in Figure 4 (a). After reaching Point C, the final detachment of BFRP sheet was observed. The entire debonding process completed at around 600 s.

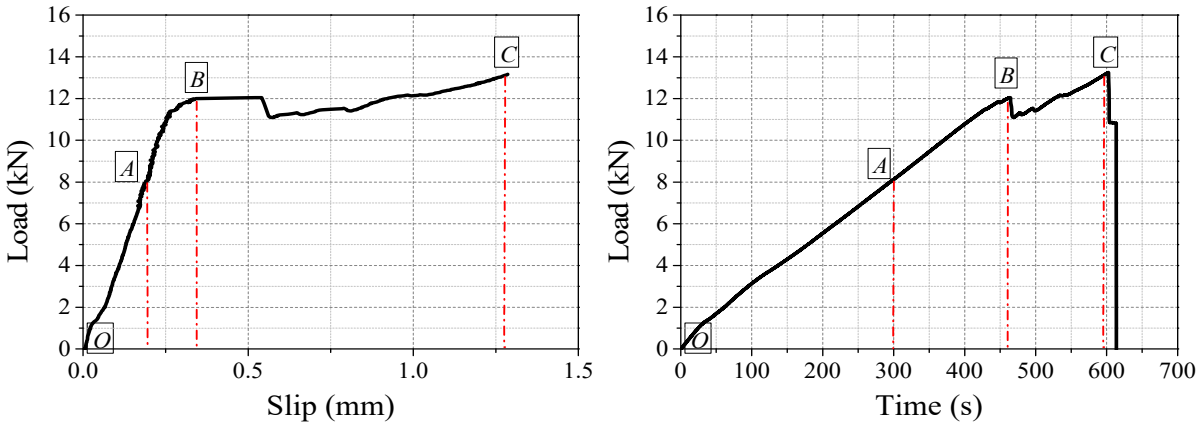

Figure 4. (a) Load-slip curve; and (b) Load-time curve

4.2 Interfacial damage identification

The tested specimen experienced a sudden failure with a flake of concrete generated beneath the BFRP sheet. Figure 5 shows the typical failure mode after the final detachment. It was observed that all the debonding failures initiated and propagated inside the concrete substrate layer. As the single-lap shear testing method was employed in this testing program, the effect of normal stress on the debonding was marginal. The debonding of BFRP-concrete interface initiated from the adhesive layer and penetrated into the concrete layer upon tensile loading. The shear stress at the interface was transformed into tensile stress and compressive stress along 45^{o} plane [25]. As tensile strength of concrete was much weaker than its compressive strength, debonding damage always initiated from the tensile side of the strengthened concrete element. Therefore, the detected local bond-slip by the SAs was actually caused by the fracture of concrete for BFRP-strengthened concrete structures.

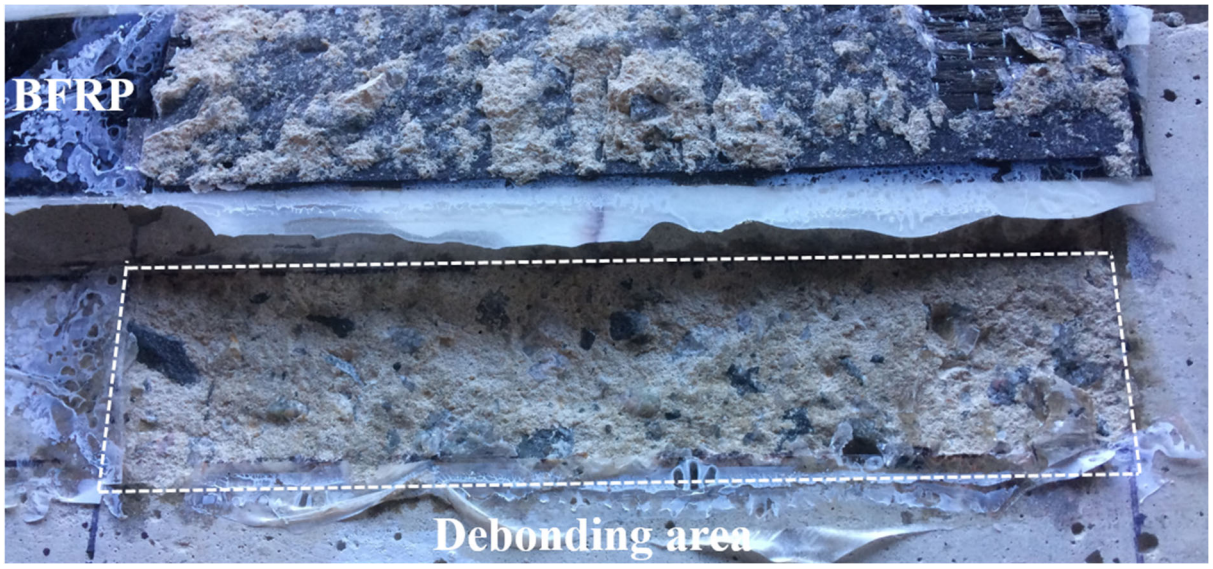

Figure 5. Failure mode of the tested specimen

Figure 6 illustrates the wave signals detected by SA-1-1 and SA-2-1, respectively. The curves with different colours represent the received signals at different bond-slip stages. The black curve refers to the healthy state of the interface at the initial loading stage (i.e. Point O in Figure 4). At the instant of debonding initiation, i.e., Point B in Figure 4, interfacial debonding occurred at the SA-1-1 location, resulting in a significant decrease of the signal amplitude (i.e. the brown curves). However, there was no obvious decrease in the signal detected by SA-2-1 sensor at the free end at this moment as debonding initiated from the loaded end and has yet propagated to the free end. SA-2-1 sensor only showed a slight reduction of signal amplitude at the instant corresponding to Point B as compared to the instant of Point A due to the microcracking damage. After initiation, the debonding propagated and passed the location of SA-2-1. Both SA sensors measured noise signal (i.e. the yellow curves) due to the full debonding. In the subsequent section, the amplitude attenuation is quantified through wavelet packet-based debonding damage index.

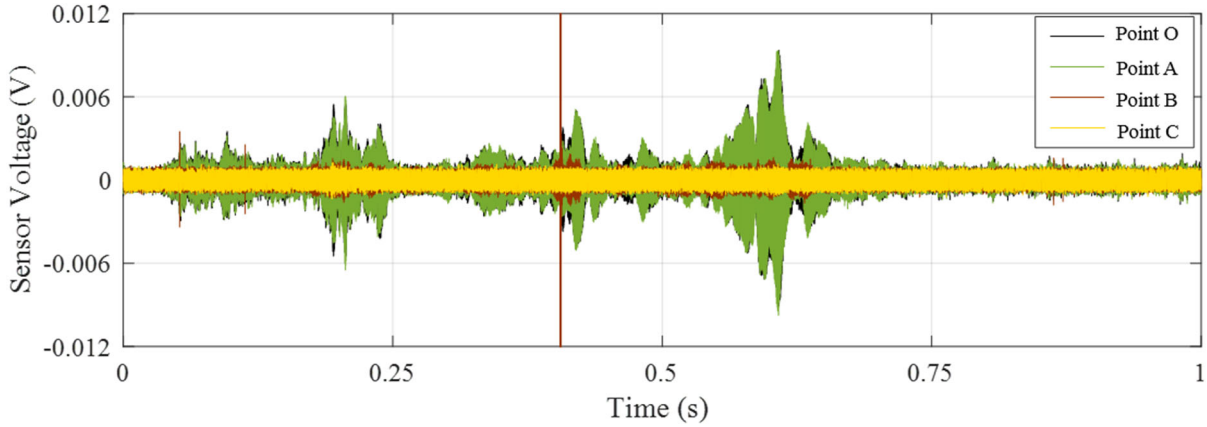

(a) SA-1-1

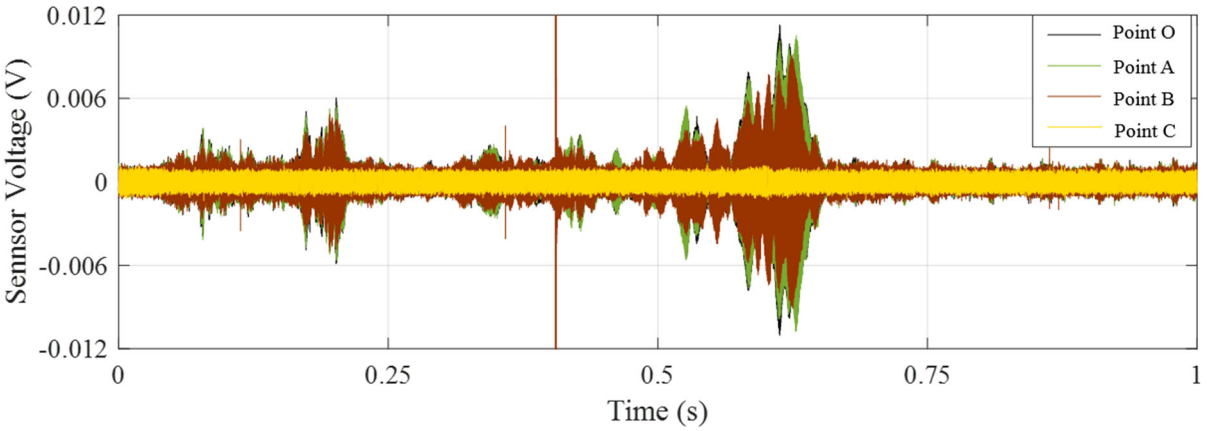

(b) SA-2-1

Figure 6. Received signals of SA sensors at different debonding stages (note: Points O/A/B/C refer to Figure 4)

Figure 7 illustrates the computed debonding damage indices for SA-1-1 and SA-2-1, as well as the shear slip contours of the BFRP sheet at four important instants of the debonding process. At the very beginning of the test, there was no debonding, so that he debonding index values for both SA-1-1 and SA-2-1 were close to zero. As shown in the shear slip contours from the DIC analysis, SA-1-1 firstly experienced the local bond-slip damage at Point A because the shear slip contours consisting of yellow and green colours covered the SA-1-1. However, no stress was transmitted to the SA-2-1 yet as shown in the colour of dark blue, which represents the zero slippage. The debonding damage index for SA-1-1 increased up to 0.2, while the value for SA-2-1 was still close to zero. With the increase of the applied tensile load, the interface experienced more damage and the debonding continued to propagate along the interface. The shear slip contours consisting of red, yellow and green colours covered both SAs at Point B,

indicating that the debonding has passed the location of SA-2-1. It can be seen from the damage indices of SA-2-1 that the index value increased up to 0.2 at Point B, indicating the initial debonding occurred at the location of SA-2-1. After that, the damage index of both SAs increased sharply to the peak value, indicating that the BFRP-to-concrete interface was fully debonded.

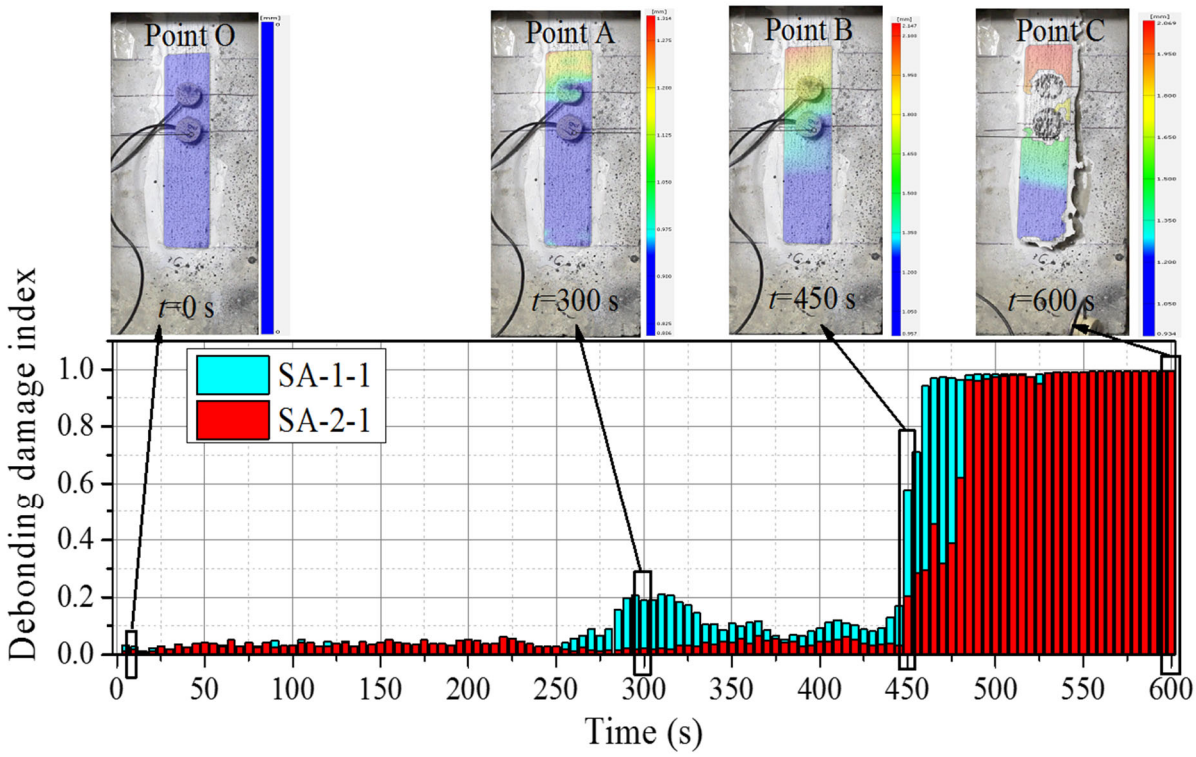

Figure 7. Shear slip and debonding damage index

Figure 8 (a, b) shows the relationship between debonding damage index and debonding load as well as shear slip of SA-1-1 and SA-2-1, respectively. It is observed that the debonding of BFRP-strengthened concrete elements is very brittle due to the sharp increment of the damage index after initial debonding stage (i.e. 450 s). As shown in Figure 8 (a), the damage index of SA-1-1 and SA-2-1 is close to zero before reaching the microcracking stage, indicating that the BFRP sheet and concrete interface is still well bonded and consequently the state of wave propagation is the same as those in the healthy state. The SA-1-1 first detected the initial damage at the loading force of 6.5 kN, indicating that the interface between BFRP and concrete

experienced concrete microcracking with local bond-slip damage, which resulted in the attenuation of wave propagation. With the increase in the applied load, the damage index of SA-1-1 increased to the range from 0.1 to 0.2 after the moment of 250 s. However, the damage index of SA-1-1 slightly reduced after the loading of 8.2 kN. This is because the microcracks in the concrete were suppressed by the applied load along the in-plane direction. The SA-2-1 is still in the healthy state before the moment of 450 s, indicating that there is marginal local bond-slip damage in its vicinity. However, the damage index of SA-2-1 increases up to 0.2 at the moment of 450 s and continues to increase until the final debonding. Figure 8 (b) illustrates the relationship between the damage index and shear slip, which is similar to the relationship between the damage index and debonding load. It can be found that the debonding detection of the SA-2-1 is always delayed than that of the SA-1-1. The SA-1-1 first detected the initiation of local damage and the damage index increased sharply after the initial debonding stage (i.e. 450 s), where the shear slip was around 0.31 mm. Meanwhile, the SA-2-1 quickly sensed the brittle interfacial debonding with the attenuation of the wave propagation and the corresponding damage index increased gradually with the increasing shear slip. After the development of the local bond-slip damage within effective bond length (EBL), the debonding damage process repeated in the next EBL until the final detachment of BFRP sheet. It should be noted the detected debonding by the SAs is the local damage rather than the global damage.

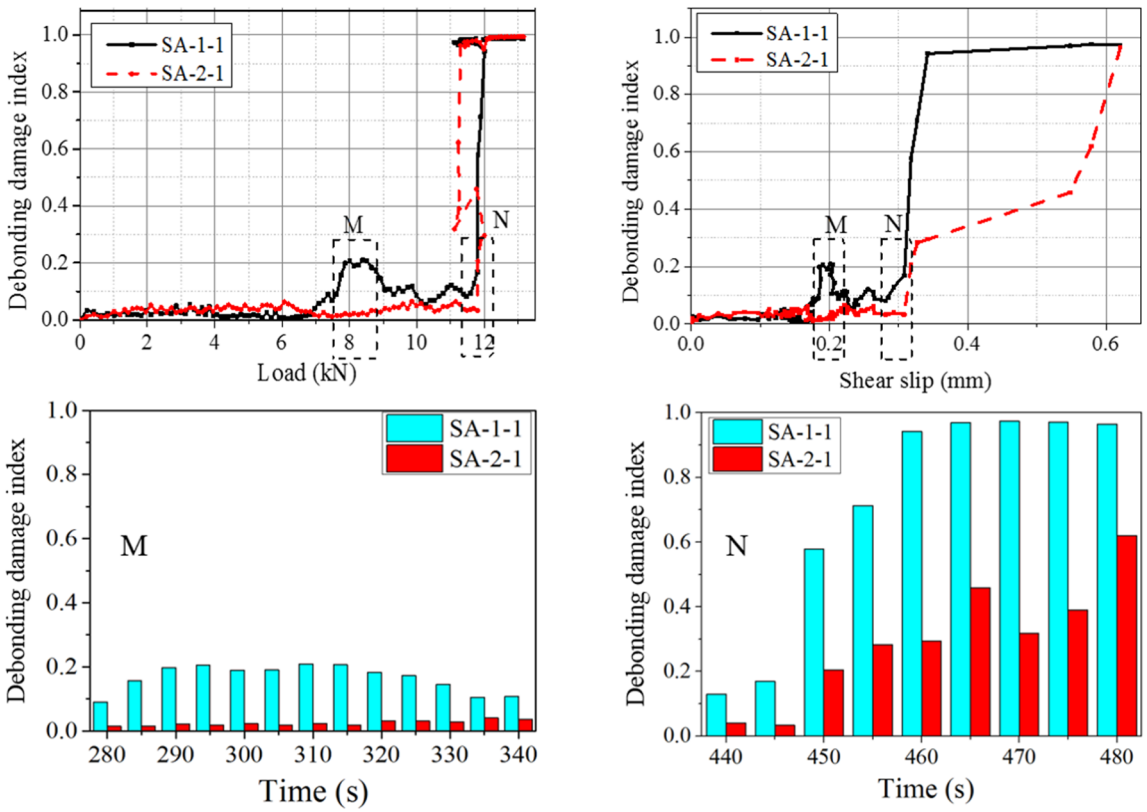

(a) (b)

Figure 8. (a) The relationship between damage index and load; and (b) The relationship between damage index and shear slip at different time instants

4.3 Interfacial bond-slip response

Figure 9 illustrates the strain contours from the DIC technique. The obtained strain contours at different damage stages consist of different colours. Red and blue colours refer to the maximum and minimum strain. At the initial debonding stage, the distance of strain transfer is known as the active stress transfer zone, which is also defined as the effective bond length (EBL). Figure 10 shows the shear slip and strain distributions of the tested specimen at different time instants, which provides a global insight of the pre-debonding and post-debonding process. The obtained shear slip is derived from the DIC analysis. The shear slip maintains a similar shape for debonding propagation. With the increase of the applied load, the shear slip increases until the final detachment. At the moments of 300 s and 450 s, the maximum shear slip is around 0.2 mm and 0.31 mm, respectively, which match well with the results provided in Figure 8 (b). To

better understand the shear stress transfer mechanism from the BFRP sheet to the concrete element, the strain profile is obtained for the shear stress propagation. It is observed that the strain maintains a similar shape for the debonding propagation after the initial debonding stage (i.e. 450 s), this is consistent with the previous studies [9]. The discontinued parts of the curves are shown in Figure 10 (a) and (b) as the areas covered by two SAs cannot be captured by DIC technique.

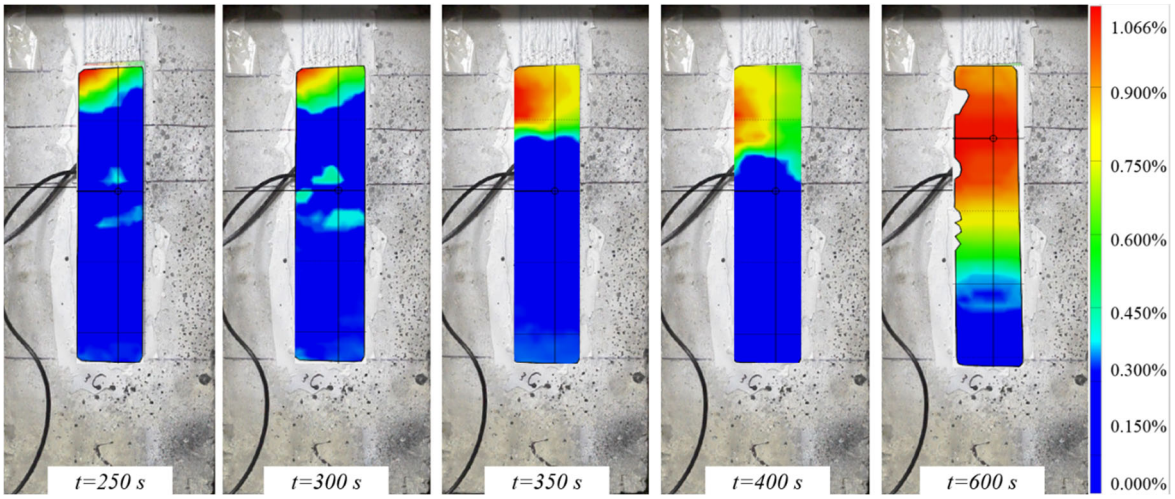

Figure 9. Strain contours at different time instants

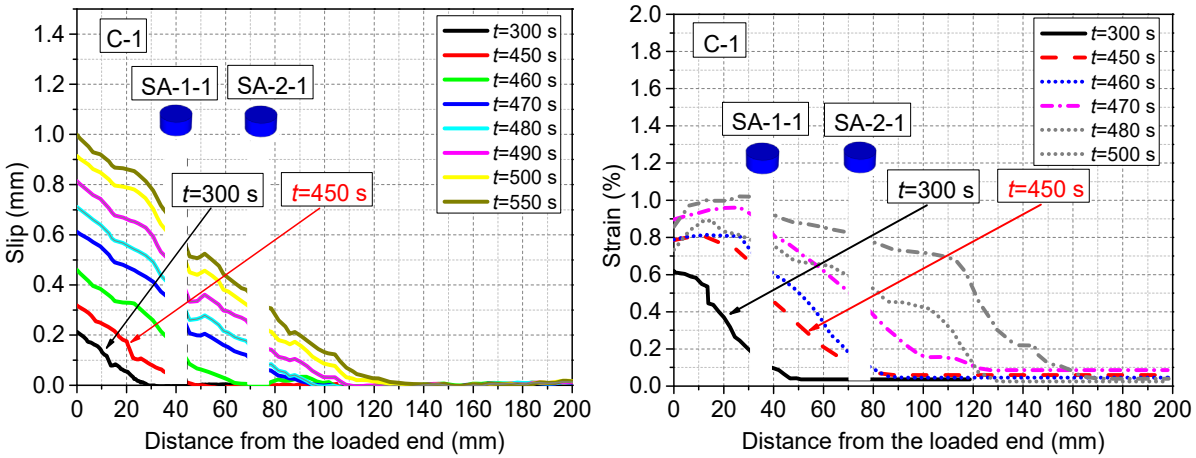

(a) Slip distribution (b) Strain distribution

Figure 10. Shear slip and strain distributions

To quantify the local bond-slip response of the interface, the shear stress can be derived using the measured strain by the following formula [9, 26]:

$$\tau(x) = \frac{\varepsilon_{k+1} - \varepsilon_k}{dx} E_f t_f \quad (5)$$

in which E_f and t_f are the elastic modulus and thickness of the BFRP sheet, respectively, $\varepsilon_{k+1} - \varepsilon_k$ refers to the strain difference between two sets (k+1 and k) on the BFRP sheet, and dx is the distance between the set $k+1$ and the set k. Figure 11 illustrates the bond-slip response of the tested specimen at different time instants. It is observed that the bond-slip responses show an ascending branch before the peak shear stress, and a descending branch is observed after the peak value. The average peak shear stress is around 5.6 MPa for the tested specimen. Three regions can be identified for the local bond-slip response, i.e. the interfacial elastic stage of the ascending branch (OA), the interfacial softening stage caused by the microcracking of concrete (AB) and the debonding stage (BC). Using the obtained debonding damage index, the SA-based active sensing process can well quantify the damage level of the elastic, microcracking and debonding stages. The quantified damage index for the microcracking stage is around 0.2, which is reasonable due to the fact that the microcracking of concrete results in a slight attenuation of stress wave energy.

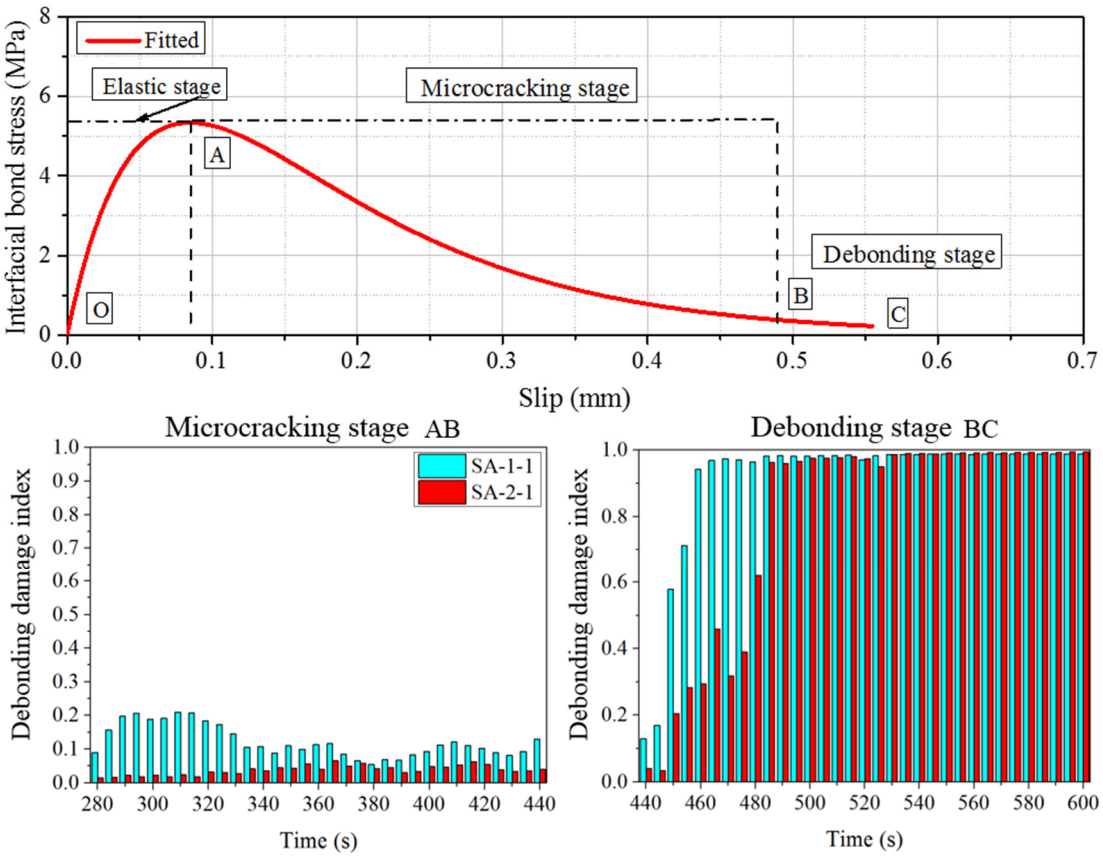

Figure 11. Bond-slip response and debonding damage index

5. Numerical validation

To further investigate the effect of BFRP debonding on the stress wave energy attenuation at the BFRP-to-concrete interface, a 3D finite element model of BFRP-to-concrete interface was built by using Abaqus commercial package. Figure 12 (a) shows the sketch of the numerical model. The BFRP sheet was tied to the concrete surface since the debonding always initiated from concrete with local bond-slip. One damaged condition of the BFRP-to-concrete interface was considered to investigate the effect of debonding cracking on the attenuation of the stress wave energy by notching the concrete beneath the BFRP sheet. Healthy condition without concrete damage was designed to simulate the healthy state of the interface and damaged condition with 40 (length) x 40 (width) x 5 (depth) mm notch of concrete was designed to simulate the initial debonding damage, as shown in Figure 12 (b). The corresponding material properties of BFRP sheet and concrete are summarized in Table 1.

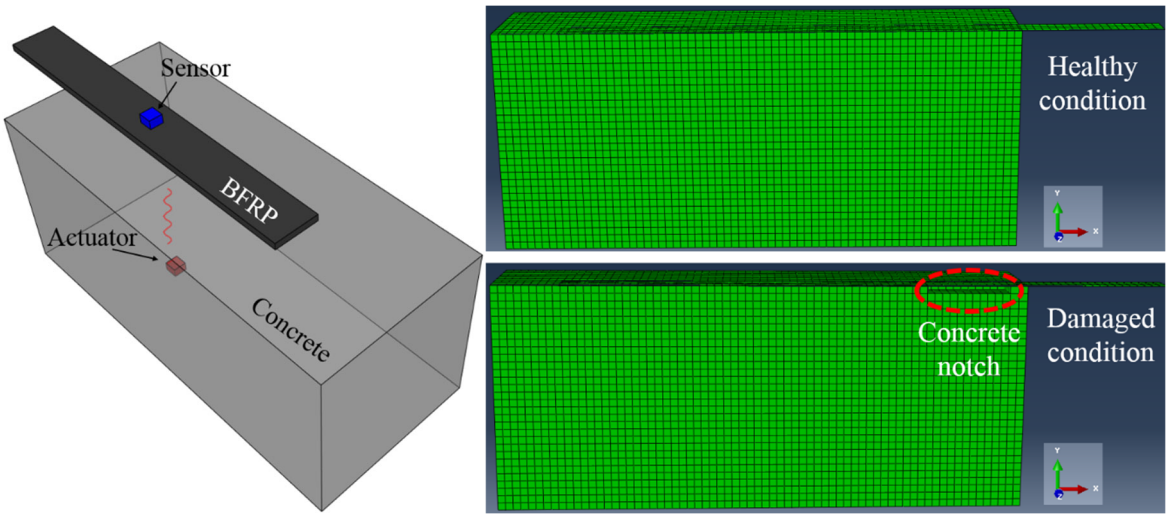

(a) Sketch of the model (b) Two conditions

Figure 12. Schematic diagram and numerical models

Table 1. Material properties.

Material	Properties	Values
BFRP	Density	1700 kg/m^3
	Poisson ratio	0.36
	Elastic modulus	73 GPa
Concrete	Density	2400 kg/m^3
	Poisson ratio	0.20
	Compressive strength	40 MPa

Harmonic sinusoidal input signal with the frequency of 100 kHz (two cycles) was used for the numerical study, instead of the swept sine wave input signal which was used in the experimental study. Song et al. [27] investigated the effect of actuation frequency from 10 to 180 kHz on the sensor response and found that the range of 90-110 kHz resulted in the strongest sensor response. Therefore, 100 kHz was selected as the actuating frequency in the numerical simulation. The wave propagation derived from the numerical model at the same moment is shown in Figure 13 (a) and (b). It is observed that the propagation of stress wave at the damaged interface is different from that in the healthy interface. For the damaged interface, the stress wave cannot propagate through the crack (i.e. notch) due to the presence of the air gap and thus form a reflected wave, which is different from the transmission of the stress wave at the healthy

interface. This can be verified by the stress wave colour map as shown in Figure 13 (a) and (b), e.g. the red colour region at the edge of notch of the damaged interface. The travelling wave signal passing two different debonding states can be obtained and the amplitudes of the received signal in different debonding states are plotted in Figure 14. The general trend of the testing results shows that the received signal is sensitive to the interfacial debonding condition. The stress wave propagation across the BFRP-to-concrete interface is weakened by the interfacial debonding. The increased debonding damage level leads to the reduction of the amplitude of the received signal.

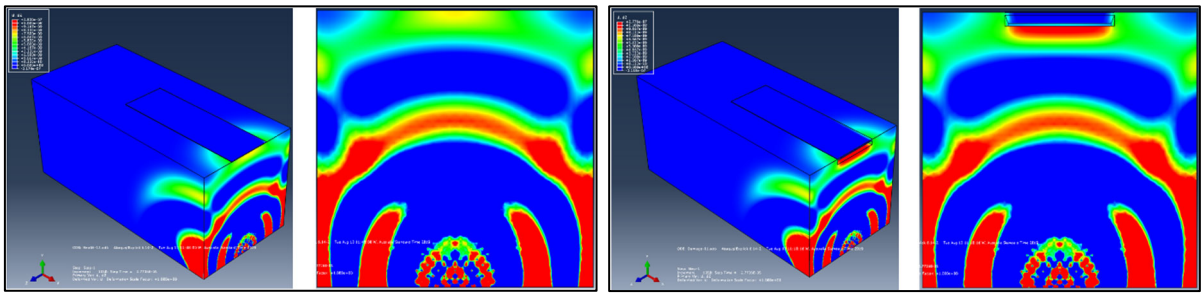

(a) (b)

Figure 13. Stress wave propagation: (a) Stress wave propagation through healthy BFRP-concrete interface; and (b) Stress wave propagation through debonded BFRP-concrete interface

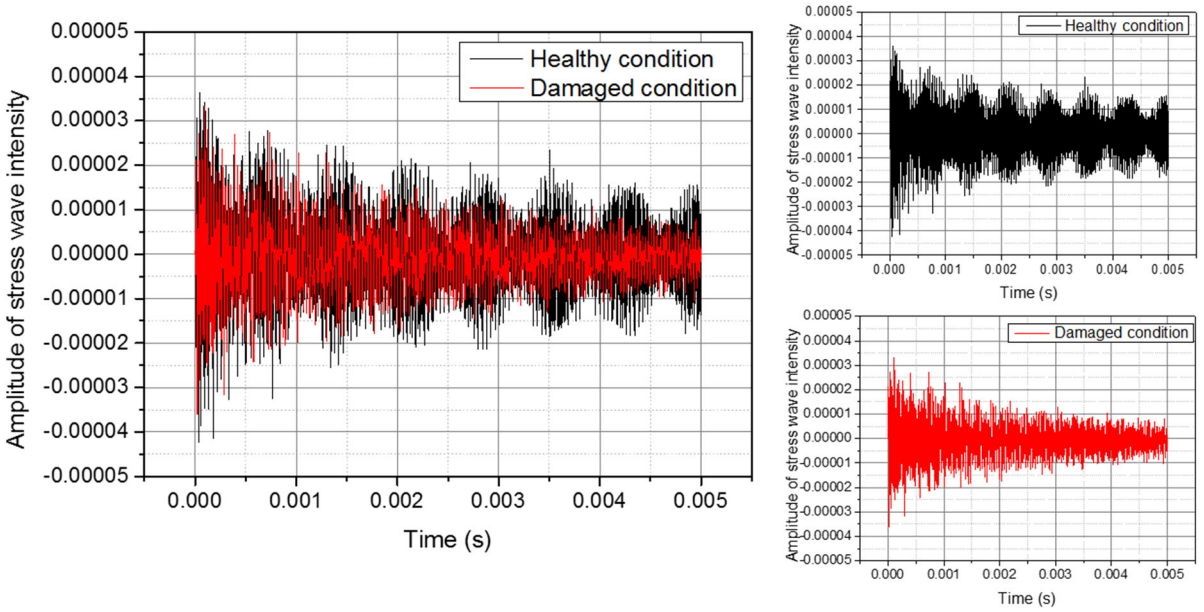

Figure 14. Comparison of amplitude of the stress wave intensity (100 kHz) under healthy and damaged conditions

6. Conclusions

In this study, the single-lap shear test was carried out to simulate the BFRP debonding from concrete element. The SA-based active sensing approach was developed to monitor the interfacial debonding of the FRP-concrete interface. The wavelet packet-based debonding damage index can successfully quantify the interfacial debonding damage level and its validity was verified by the digital image correlation (DIC) measurement. In addition, as validated by the numerical results, the obtained debonding damage index can represent the interfacial damage level. As single SA pair can only detect the local damage, multiple SA pairs are suggested to be used for extending the detected range from local to global. The developed method in this study provides alternative solution for fast detection and real-time monitoring of FRP-concrete interfacial debonding in engineering practice.

Acknowledgement

The authors thank Australian Research Council Linkage Project (ARC LP150100259) and Chinese State Key Laboratory of High Performance Civil Engineering Materials (2018CEM003) for the financial support.

References

[1] Wu Y-F, Jiang C. Quantification of bond-slip relationship for externally bonded FRP-to-concrete joints. Journal of Composites for Construction. 2013;17:673-86.
[2] Smith ST, Zhang H, Wang Z. Influence of FRP anchors on the strength and ductility of FRP-strengthened RC slabs. Construction and Building Materials. 2013;49:998-1012.
[3] Chen W, Hao H, Jong M, Cui J, Shi Y, Chen L, et al. Quasi-static and dynamic tensile properties of basalt fibre reinforced polymer. Composites Part B: Engineering. 2017;125:123-33.
[4] Chen W, Pham TM, Sichembe H, Chen L, Hao H. Experimental study of flexural behaviour of RC beams strengthened by longitudinal and U-shaped basalt FRP sheet. Composites Part B: Engineering. 2018;134:114-26.
[5] Jiang J-F, Wu Y-F. Plasticity-based criterion for confinement design of FRP jacketed concrete columns. Materials and Structures. 2016;49:2035-51.
[6] Yuan C, Chen W, Pham TM, Chen L, Cui J, Shi Y, et al. Effect of aggregate size on the dynamic interfacial bond behaviour between basalt fiber reinforced polymer sheets and concrete. Construction and Building Materials. 2019;227:116584.

[7] Zhang D, Gu X-L, Yu Q-Q, Huang H, Wan B, Jiang C. Fully probabilistic analysis of FRP-to-concrete bonded joints considering model uncertainty. Composite Structures. 2018;185:786-806.
[8] Zhang H, Smith ST, Gravina RJ, Wang Z. Modelling of FRP-concrete bonded interfaces containing FRP anchors. Construction and Building Materials. 2017;139:394-402.
[9] Wu Y-F, He L. Width effect of interfacial bond characteristics. Construction and Building Materials. 2019;220:712-26.
[10] Jiang C, Wan B, Wu Y-F, Omboko J. Epoxy interlocking: A novel approach to enhance FRP-to-concrete bond behavior. Construction and Building Materials. 2018;193:643-53.
[11] Yuan C, Chen W, Pham TM, Hao H. Bond behavior between basalt fibres reinforced polymer sheets and steel fibres reinforced concrete. Engineering structures. 2018;176:812-24.
[12] Yuan C, Chen W, Pham TM, Hao H, Cui J, Shi Y. Strain rate effect on interfacial bond behaviour between BFRP sheets and steel fibre reinforced concrete. Composites Part B: Engineering. 2019:107032.
[13] Yuan C, Chen W, Pham TM, Hao H. Effect of aggregate size on bond behaviour between basalt fibre reinforced polymer sheets and concrete. Composites Part B: Engineering. 2019;158:459-74.
[14] Jiang J, Luo J, Yu J, Wang Z. Performance Improvement of a Fiber-Reinforced Polymer Bar for a Reinforced Sea Sand and Seawater Concrete Beam in the Serviceability Limit State. Sensors. 2019;19:654.
[15] He J, Yuan F-G. Lamb wave-based subwavelength damage imaging using the DORT-MUSIC technique in metallic plates. Structural Health Monitoring. 2016;15:65-80.
[16] Ong WH, Rajic N, Chiu WK, Rosalie C. Lamb wave–based detection of a controlled disbond in a lap joint. Structural Health Monitoring. 2018;17:668-83.
[17] Giri P, Kharkovsky S, Zhu X, Clark SM, Taheri S, Samali B. Characterization of carbon fiber reinforced polymer strengthened concrete and gap detection with a piezoelectric-based sensory technique. Structural Health Monitoring. 2019;18:172-9.
[18] Beale C, Willis DJ, Niezrecki C, Inalpolat M. Passive acoustic damage detection of structural cavities using flow-induced acoustic excitations. Structural Health Monitoring. 2019:1475921719860389.
[19] Arora V, Wijnant YH, de Boer A. Acoustic-based damage detection method. Applied acoustics. 2014;80:23-7.
[20] Poozesh P, Aizawa K, Niezrecki C, Baqersad J, Inalpolat M, Heilmann G. Structural health monitoring of wind turbine blades using acoustic microphone array. Structural Health Monitoring. 2017;16:471-85.
[21] Zhu J, Ren L, Ho S-C, Jia Z, Song G. Gas pipeline leakage detection based on PZT sensors. Smart Materials and Structures. 2017;26:025022.
[22] Yao P, Kong Q, Xu K, Jiang T, Huo L-s, Song G. Structural health monitoring of multi-spot welded joints using a lead zirconate titanate based active sensing approach. Smart Materials and Structures. 2015;25:015031.
[23] Kong Q, Song G. A comparative study of the very early age cement hydration monitoring using compressive and shear mode smart aggregates. IEEE Sensors Journal. 2016;17:256-60.
[24] Xu B, Li B, Song G. Active debonding detection for large rectangular CFSTs based on wavelet packet energy spectrum with piezoceramics. Journal of Structural Engineering. 2012;139:1435-43.
[25] Salimian MS, Mostofinejad D. Experimental Evaluation of CFRP-Concrete Bond Behavior under High Loading Rates Using Particle Image Velocimetry Method. Journal of Composites for Construction. 2019;23:04019010.

[26] Dai JG, Ueda T, Sato Y. Development of the nonlinear bond stress–slip model of fiber reinforced plastics sheet–concrete interfaces with a simple method. Journal of Composites for Construction. 2005;9:52-62.
[27] Song F, Huang G, Kim J, Haran S. On the study of surface wave propagation in concrete structures using a piezoelectric actuator/sensor system. Smart Materials and Structures. 2008;17:055024.